energies

MDPI

Article

Lithium Battery Model and Its Application to Parallel Charging

Yueh-Tsung Shieh [1], Chih-Chiang Wu [2], Ching-Yao Liu [1], Wei-Hua Chieng [1,*], Yu-Sheng Su [3], Shyr-Long Jeng [4] and Edward-Yi Chang [5]

[1] Department of Mechanical Engineering, College of Engineering, National Yang Ming Chiao Tung University, Hsinchu 30010, Taiwan; onion0720.me09g@nctu.edu.tw (Y.-T.S.); liucy721.me09g@nctu.edu.tw (C.-Y.L.)
[2] Mechanical and Mechatronics Systems Research Laboratories, Industrial Technology Research Institute, Hsinchu 31040, Taiwan; john.wu@itri.org.tw
[3] International College of Semiconductor Technology, National Yang Ming Chiao Tung University, Hsinchu 30010, Taiwan; yushengsu@nycu.edu.tw
[4] Department of Mechanical Engineering, Lunghwa University of Science and Technology, Taoyuan City 33306, Taiwan; aetsl@gm.lhu.edu.tw
[5] Department of Material Science and Engineering, College of Engineering, National Yang Ming Chiao Tung University, Hsinchu 30010, Taiwan; edc@mail.nctu.edu.tw
* Correspondence: whc@cc.nctu.edu.tw; Tel.: +886-3-571-2121 (ext. 55152)

Abstract: A new *SOC* (State-Of-Charge)–VOC (Voltage-of-Open-Circuit) mathematical model was proposed in this paper, which is particularly useful in parallel lithium battery modeling. When the battery strings are charged in parallel connection, the batteries can be deemed as capacitors with different capacitances, and the one with larger capacitance always obtains the higher current. According to this mathematical model, the parallel battery charging with different peak capacitances can result in different voltage slew rates on different battery strings during the constant current control. Different parallel battery strings are charged with different currents, of which the battery string under higher current can induce higher power loss and higher temperature. The conventional solution can use this model to switch the constant current charging into the constant voltage charging with the correct timing to avoid overcurrent charging. Other battery pack protection methods including current sense resistor, resettable thermal cutoff device, or resettable fuse can also use this mathematical model to improve the protection. In the experiments, three kinds of batteries including $LiFePO_4$ battery, EV Type-1 battery, and ternary battery were examined. The experiments showed good consistency with the simulation results derived from the mathematical model.

Keywords: battery modeling; parallel charging; *SOC*–VOC

Citation: Shieh, Y.-T.; Wu, C.-C.; Liu, C.-Y.; Chieng, W.-H.; Su, Y.-S.; Jeng, S.-L.; Chang, E.-Y. Lithium Battery Model and Its Application to Parallel Charging. *Energies* **2022**, *15*, 4767. https://doi.org/10.3390/en15134767

Academic Editors: Emad Manla and Behnam Askarian

Received: 12 June 2022
Accepted: 27 June 2022
Published: 29 June 2022

1. Introduction

To meet the requirements for power and energy, cells connected in parallel and in series in a battery pack are required. Cells connected in parallel or in series bring some battery charging and energy balancing issues. Some papers explore the impact of parallel connecting cells with varied properties, and introduce a model for serial-connected [1] or parallel-connected cells [2] in a battery pack. Current differences in parallel connecting can cause differences in the state of charge, temperature, and degradation rate of each cell. Several existing battery-charging [3,4] and cell-balancing [5,6] techniques with flyback-based converters are well presented. The flyback converter has been widely adopted for lithium-based batteries in electrical vehicles because of its simple structure and high conversion efficiency [3–6].

There are several methods proposed for *SOC* estimation, such as the open-circuit voltage method, coulomb counting methods, machine learning method, and model-based method [7,8]. Among these methods, the open-circuit voltage method has high precision and simple implementation, so it is suitable for *SOC* estimation. Accurate VOC plays an important role to estimate *SOC*. There are several fitting methods [1,8–11] for *SOC*–VOC

voltage characteristics, including polynomial functions [8,10], sigmoid fitting functions [11], and complex fitting functions [11]. In ref. [8], an 8th degree polynomial fitting function using the genetic algorithm was used to establish the relationship between VOC and *SOC* mapping. In ref. [10], nonlinear semi-infinite programming polynomial model was proposed and showed accurate *SOC* estimation in comparison with the traditional polynomial and sigmoid models. The complex VOC curve can be fitted by using high-order polynomial models. In ref. [11], a unified VOC model using sigmoid function was presented for both *SOC* estimation and SOH monitoring. Moreover, in ref. [1], a dual-scale cell *SOC* estimation complex fitting function was proposed for series-connected battery pack. For optimizing the complex parameters, the machine learning [12] and artificial intelligence [13] method can be used to help training data in battery models. Due to the complexity of the parameters obtained from abovementioned literatures, the shifted sigmoid *SOC*–VOC model was proposed and derived for estimating *SOC* in this work.

The purpose of this paper was to provide a new *SOC*–VOC mathematical model for the parallel lithium battery charging analysis. Three kinds of batteries including the $LiFePO_4$ battery, the EV Type-1 battery, and the ternary battery were tested and used to verify the proposed model for *SOC* estimation. This study is organized as follows. First, the battery charger including battery characteristics, battery management system, and two kinds of battery charge structures, interleaved and multi-winding flyback converter, for parallel and series connected are introduced in Section 2. Then, the shifted sigmoid *SOC*–VOC model and model fitting are shown in Section 3. Furthermore, constant current charging, and charging parallel, connected batteries are also discussed in this section. Simulation and experiment are shown in Section 4. At last, the conclusions of this work are summarized in Section 5.

2. Battery Charger

The flyback converter can be used in the battery charger of PV, EV, and other battery applications. Low-rate battery chargers may take several hours to complete a charge. Fast chargers may restore most capacity, but the application of high rate chargers can be limited by battery types such as lithium batteries. Such batteries require active monitoring to protect them from overcharging. Electric vehicles ideally need fast charging. For public access, installation of such fast chargers including the distribution support is a critical issue for the supplier. Charging batteries in the right manner is key to maintaining their performance, which is required to ensure a higher level of performance and a longer life.

2.1. Battery Characteristics

For commercial EV lithium batteries, they can be categorized into two major battery chemistries, ternary and $LiFePO_4$ [14]. Ternary lithium batteries adopt layer oxide cathode material such as lithium nickel–cobalt–manganese (NCM: $LiNi_{1-x-y}Co_xMn_yO_2$) and lithium nickel–cobalt–aluminum (NCA: $LiNi_{1-x-y}Co_xAl_yO_2$). The advantages of using ternary cathodes are high specific capacity, low internal resistance, and good structural stability [15]. By increasing the nickel content in ternary cathode materials, their specific capacity can be boosted to over 200 mAh g^{-1} (NCM811 or NCM955) [15], which are very popular in advanced EV batteries. NCA-80 ($LiNi_{0.8}Co_{0.15}Al_{0.05}O_2$), majorly used by Tesla, has a comparable capacity to NCM811, but with better capacity retention and enhanced thermal stability due to the removal of manganese ion dissolution in the electrolyte [15]. In terms of battery cell types, cylindrical, pouch, and prismatic are three major forms in battery cell manufacturing [16]. Cylindrical cells have industrial standard specifications, such as 18,650, 21,700, and 4680, which are determined by the cell diameter and height. The energy-type cells are made with thicker electrodes to contain more active materials, and the power-type cells are made with thinner electrodes and more conductive tabs to reduce electrical and ionic resistances and improve power density. In this report, we tested standard rechargeable 18,650 cells (a + plus ICR186500-26) that have a terminal voltage of 3.7 V and specific capacity of 2600 mAh. Different from the $LiFePO_4$ battery with a flat

discharge plateau at around 3.2–3.3 V, the ternary battery has a sloping discharge curve from 4.2–2.6 V but a better energy density.

2.2. Battery Management System

The battery management system (BMS) is used to monitor battery state and ensure the safety of charging and discharging operations [17]. BMS equipped with electronic switches is commanded to disconnect the batteries from charger or load under defined critical conditions. One of the critical conditions is the over current condition that the battery cell is exposed to a high inrush charging current or outrush discharging current, which leads to the overheating of the batteries. During the charging of multi-module batteries, which consist of several single-battery modules connected in series or parallel, the inrush current limiting circuit that limits the current during the turn-on phase and protects both the battery and the load is necessary. In the battery charging stage, the batteries in parallel can be equalized using the interleave circuit to avoid the inrush current due to the instantaneous capacitance differences among the batteries. At the same time, the series connected batteries can be equalized using the multi-winding transformer in flyback converter to maintain each individual battery module at the same charge level.

2.3. Interleaved Flyback Converter for Battery Charging

In interleaved flyback converter [18], two replicated sets of flyback converters are connected in parallel as shown in Figure 1. The two converters in alternative operating modes can yield the best power efficiency under heavily loaded conditions since the switching losses of the power switches and other losses are reduced. Higher efficiency during heavily loaded conditions can be achieved by sharing the current equally between the two replicated converters and reduce the current square losses. Ideally, if both the flyback converters can be operated in the BCM mode, then they may be able to share the same magnetic core to reduce the size of the transformer. However, in practice, with the batteries having large capacitances, the current flow can be noisy during diode turn-off and primary inductor charging periods. The magnetism becomes much more complicated than the single flyback structure. Passive lossless snubbers, which are more reliable and easy to implement, are more preferred to be used for suppressing switching losses. However, ZVS and ZCS conditions at turn off and turn on instants for the converter switch can only be implemented in the DCM operations.

2.4. Multi-Winding Flyback Converter for Battery Charging

The multi-winding flyback topology [3] for battery-charger applications which require a total output power level of approximately 200 W is shown in Figure 2. The design is specified for 12 V output voltage as required for a 3-cell Li-ion battery charger. The individual secondary windings are of 10 ampere output current. The diodes of the secondary windings are initially off when the primary winding is charging the current into the magnetic field and then the magnetic energy is shuffled to the battery through the secondary winding. In this multi-winding arrangement, all secondary voltages are the same as they share the same flux linkage when the magnetic circuit of the secondary sides are identical.

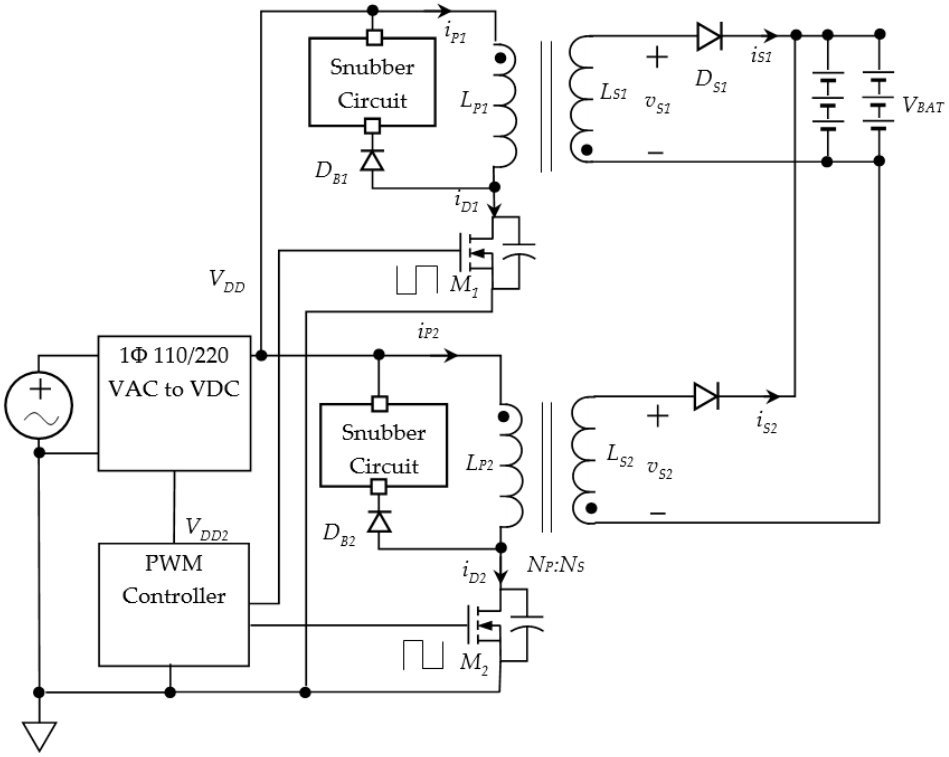

Figure 1. Interleaved flyback converter.

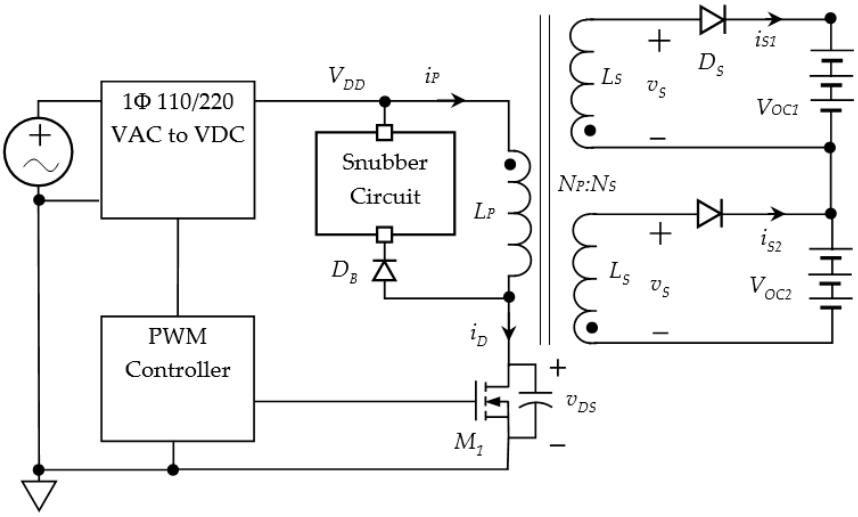

Figure 2. Multi-winding flyback converter.

3. Battery Charging Model

The electrical model is conventionally described by an equivalent circuit based on a combination of basic elements, such as voltage sources, resistors, and capacitors, to approximate the electrochemical processes and input-to-output dynamics of the battery. Combining the passive components in different ways, the researchers constructed the electrical models into Thevenin equivalent circuit model, Rint model, radio control model, and table lookup learning model. The Thevenin equivalent circuit model is commonly suggested to simulate the lithium-ion battery as it is a simple embodiment of the battery's dynamic response within an acceptable error bound.

SOC (State-Of-Charge) is defined as the status of available energy (mAh or Ah) in the battery and usually expressed as percentages. Because the available battery energy is a function charging/discharging rate, temperatures, and battery aging effects, the *SOC*

is then defined more clearly as *ASOC* (Absolute State-Of-Charge) and *RSOC* (Relative State-Of-Charge). The range of *RSOC* is from 0% to 100%, a fully charged battery's *RSOC* is always 100%, and a fully discharged battery has 0% *RSOC*. The *ASOC* is a reference calculated by design capacity which is a fixed capacity from right after the battery is manufactured. A fully charged new battery will have *ASOC* 100%, after that it is less than 100% with the aging effect under different charge/discharge usage conditions. In order to obtain the *SOC*–VOC relationship experimentally, first we began with a blank battery and started charging it with very low C-rate to the designed open circuit voltage $V_{OC,MAX}$ until reaching a fully charge state at *ASOC* 100%. Then, once we started discharging the cell with the same low C-rate, we saw that the discharge curve was different from the charge curve, which means that for the same *SOC* level the value VOCs cannot be the same during charging and discharging because of the hysteresis characteristics, as shown in Figure 3. The hysteresis also happened for high C-rate charge and discharge. It is noted that the designed open circuit voltage $V_{OC,MAX}$ is a reference value from the manufacturer. Thus, when the battery was charged again to the voltage $V_{OC,MAX}$, the *RSOC* was no longer 100%. It will take a longer time to obtain a higher voltage of V_{OC} in order to fully charge at *RSOC* state 100%.

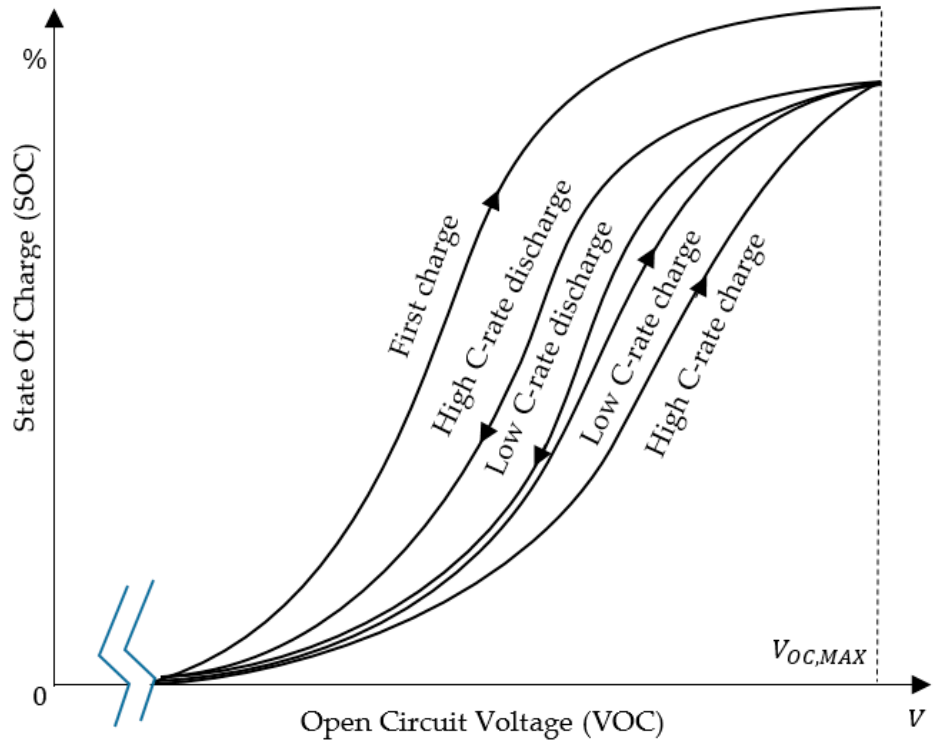

Figure 3. *SOC*–VOC chart.

3.1. Shifted Sigmoid SOC–VOC Model

The previous equivalent models are useful for the circuit simulation purpose while our *SOC*–VOC model called the shifted sigmoid model is proposed for the analysis purpose as follows.

$$g(V_{OC}) = \frac{Ke^{-\alpha V_P}}{e^{-\alpha V_{OC}} + e^{-\alpha V_P}} \quad (1)$$

V_{OC} is open circuit voltage of the battery. The *SOC* defined in this paper without further notice is the *RSOC*, which is expressed as percentage as follows

$$\begin{aligned} SOC = RSOC &= 100\% \times g(V_{OC}) \\ ASOC &= RSOC \times \frac{Q}{Q_{new}} \end{aligned} \quad (2)$$

Q_{new} denotes the capacity from right after the battery is manufactured. Q denotes the capacity of the battery. When we confine the function value that $0 \leqq g(V_{OC}) \leqq 1$, the SOC can be defined as follows.

$$g \equiv g(V_{OC}) = \frac{SOC}{100} \tag{3}$$

$V_P < V_{OC,MAX}$ is the peak capacitance voltage, which is a function of time t, temperature T, and the charging/discharging current I_{BAT}

$$V_P = V_{P0} + c_1 t + c_2 T + c_3 \times |I_{BAT}| \tag{4}$$

V_{P0} is the same as the $ASOC$ being a reference design voltage of peak capacitance which is a fixed voltage from right after the battery is manufactured. c_1 is the time drift coefficient which is typically a negative value, that is the peak capacitance voltage V_P is the decreasing function along time. c_2 is the temperature drift coefficient which is a negative coefficient for the Lithium batteries. c_3 is the current drift coefficient which is normally a negative coefficient in the Lithium batteries. K is a scaling factor to scale the maximum value of $g(V_{OC})$ to unity for SOC.

$$1 < K = 1 + e^{\alpha(V_P - V_{OC,MAX})} < 2 \tag{5}$$

The above equation may also be written as follows.

$$ln(K-1) = \alpha(V_P - V_{OC,MAX}) \tag{6}$$

K approaches 2 when small α or V_P is very closed to $V_{OC,MAX}$ while K approaches 1 when α is large. The negative coefficient terms that decrease V_P will simultaneously decrease the scaling factor K. Coefficient α is the focus factor of the capacitance. Larger value of α yields higher gradient result of $g(V_{OC})$ around $V_{OC} = V_P$. The shifted sigmoid function $g(V_{OC})$ yields the value at V_P to be exactly half of the constant K.

$$g(V_P) = \frac{K}{2} < 1 \tag{7}$$

The instantaneous change of SOC for each individual state of V_{OC} is the first derivative of sigmoid function derived as follows.

$$\frac{dg}{dV_{OC}} = g' = \alpha(K-g)g \tag{8}$$

Considering the battery is a simple capacitor and ignoring the internal resistance, we obtain a simple relation of the instantaneous capacitance of the battery as follows.

$$c = \frac{dq}{dv_{OC}} = Qg' \tag{9}$$

Q is also a reference of the state-of-health (SOH) of the battery, that is, Q will decrease through the charging/discharge cycles. That is a function of $g(V_{OC,MAX})$ as follows. The $g(V_{OC,MAX})$ was unity right after the manufacturing and is reduced along time. As shown in Figure 4, the maximum capacitance c_{max}. occurs at $V_{OC} = V_P$ and the maximum capacitance value is derived as follows.

$$c_{max} = Qg'(V_P) \tag{10}$$

From Equation (1), it is obtained that

$$g'(V_P) = \frac{\alpha K^2}{4} \tag{11}$$

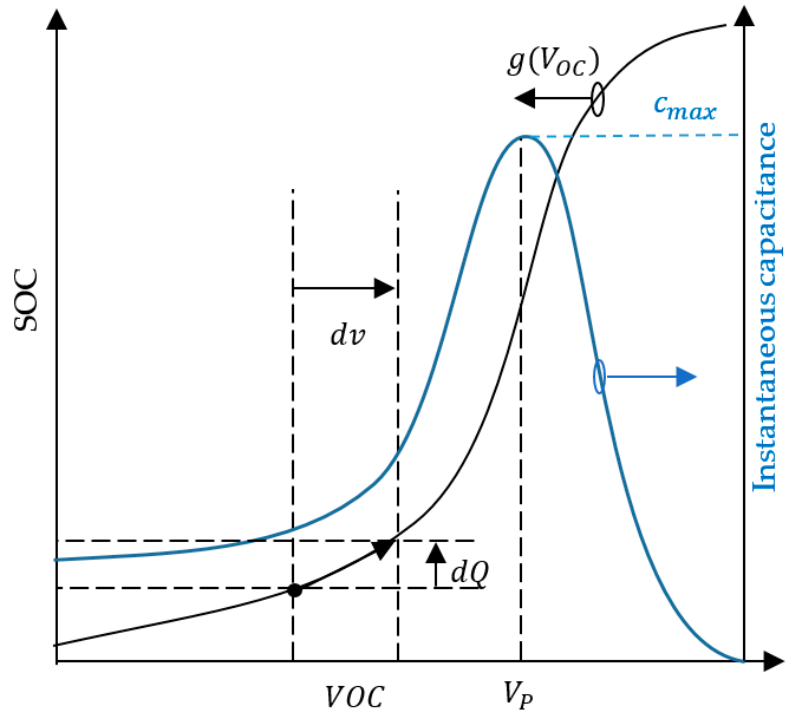

Figure 4. The shifted sigmoid and the instantaneous capacitance of the battery.

When substituting the above equation into Equation (10), we can write the focus factor α in terms of the maximum instantaneous capacitance as follows.

$$\alpha = \frac{4c_{max}}{K^2 Q} \tag{12}$$

The focus factor α linearly increases with the maximum instantaneous capacitance c_{max}. Substituting Equation (6) into (12), we can cancel out voltage amplification α and the scaling factor K is written in terms of the maximum instantaneous capacitance c_{max} and the peak capacitance voltage V_P as follows.

$$K^2 ln\left(\frac{1}{K-1}\right) = \frac{4c_{max}}{Q}(V_{OC,MAX} - V_P) \tag{13}$$

According to the result shown in Figure 5, the above equation may be simplified in different ranges. For small-capacity batteries, the approximation can be considered as follows.

$$3.2 - K(K-0.4) = \frac{4c_{max}}{Q}(V_{OC,MAX} - V_P) \quad for\ 1.2 < K < 2 \tag{14}$$

For large-capacity batteries, the approximation can be considered as follows.

$$-2.3log(K-1) = \frac{4c_{max}}{Q}(V_{OC,MAX} - V_P) \quad for\ 1 < K < 1.01 \tag{15}$$

The second derivative of the shifted sigmoid function is as follows.

$$\frac{d^2 g}{dV_{OC}{}^2} = g'' = \alpha^2 Kg(K-g)(1-2g) \tag{16}$$

The above equation implies that the inflection point is at $g(V_{OC}) = 1/2$. Due to the rapid rise of the shifted sigmoid function $g(V_{OC})$ around V_P, the inflection point may be located at V_P without much deviation. $V_{OC,MAX}$, Q, and V_P are in general the monotonic decreasing functions during the charge/discharge cycles. The maximum instantaneous

capacitance c_{max} is then the monotonic decreasing function of the charge/discharge cycles. The *SOC* approximation according to the shifted sigmoid *SOC*–VOC model is derived as follows.

$$V_{OC} = \frac{1}{\alpha} ln\left(\frac{g}{K-g}\right) + V_P \quad (17)$$

When substituting $g = K/2$ into the above equation, we obtain $V_{OC} = V_P$ which is consistent with Equation (7).

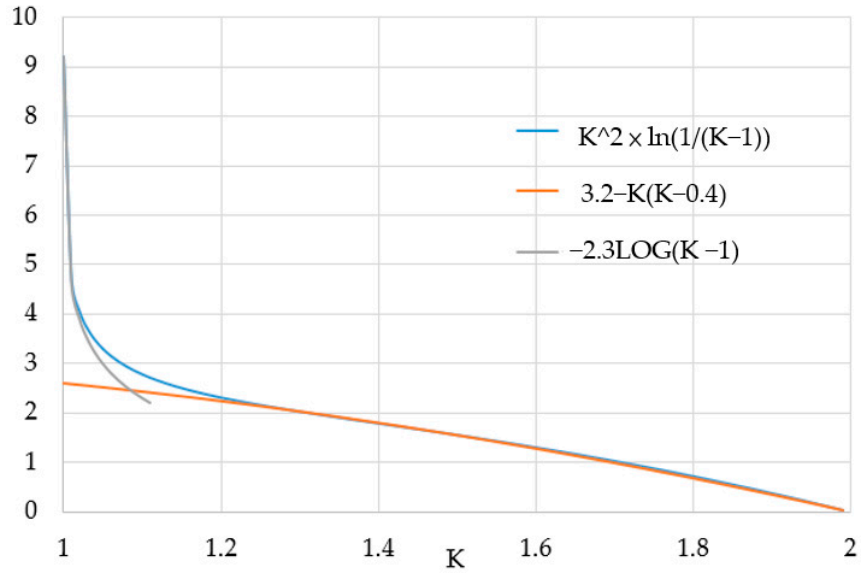

Figure 5. Linear interpolation of *K*.

3.2. SOC Model Fitting

The *SOC* model fitting is applied to two kinds of batteries including $LiFePO_4$ battery and EV Type-1 battery. Different batteries have different characteristics than one another, namely the $LiFePO_4$ battery [9] had larger maximum instantaneous capacitance c_{max}, and the EV Type-1 battery had the larger peak capacitance voltage V_P and $V_{OC,MAX}$ as well. The third kinds of the batteries, the ternary 18,650 batteries, were used in the experiment for comparing with the simulation result.

3.2.1. LiFePO4 Battery

Table 1 shows the parameters for the $LiFePO_4$ battery, in which the C_{max} was obtained from the experiments in ref. [9]. According to the parameters, we first calculated the focus factor α from the $LiFePO_4$ battery parameters based on Equation (12) providing $K = 1$ is assumed as follows.

$$\alpha = \frac{4c_{max}}{Q} = 92 \quad (18)$$

Table 1. Parameters for the $LiFePO_4$ battery [9].

Symbol	Unit	Description	Value
Q	Ah	Battery capacity	6.5
$V_{OC,MAX}$	V	Maximum Open Circuit voltage	3.65
V_P	V	Peak voltage	3.35
c_{max}	Ah/V	Maximum instantaneous Capacitance Δv_{oc} = 10 mV	150 *

*: Data obtained from ref. [9].

The scaling factor K can be solved in the range of $1 < K < 1.01$ based on Equation (15) as follows.

$$K = 1 + 10^{-\frac{4c_{max}}{2.3Q}(V_{OC,MAX} - V_P)} = 1 + 10^{-12} \tag{19}$$

The result K is very close to unity. The inflection point of the battery storage is exactly at V_P = 3.35 V. Equation (11) yields that

$$g'(V_P) = \frac{\alpha K^2}{4} = 23 \tag{20}$$

The sampling time for the experiment is untraceable due to the capacitance derivation from Equation (9) being independent of time. We plugged the focus factor α, the scaling factor K, and the peak capacitance voltage V_P into Equation (1), which yielded the result shown in Figure 6. The c_{max} determines the focus factor and the corresponding VOC-*SOC* curve was less steep when we reduced c_{max}.

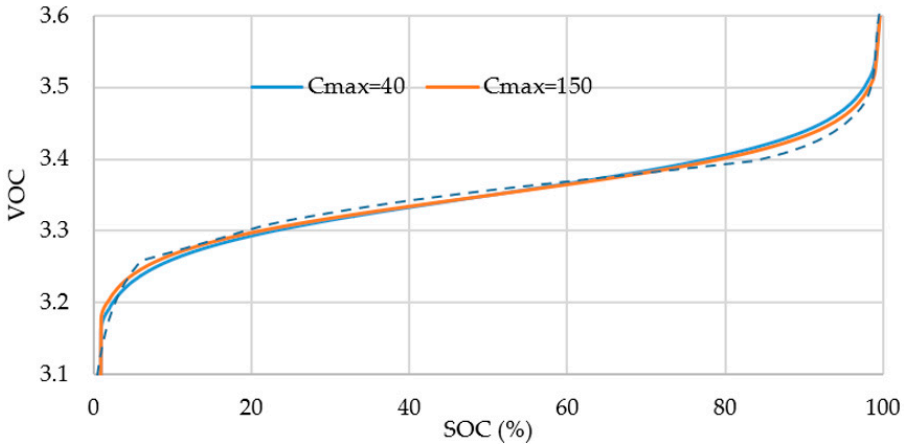

Figure 6. Model fitting of the $LiFePO_4$ battery compared with the dotted lines obtained from ref. [9].

3.2.2. EV Type-1 Battery

The dotted lines in Figure 7 shows the data generated from a Type-1 battery cycled by 0.8 C charging at 45 °C [19]. Type-1 batteries are used in the EV or PHEV such as Citroen C-Zero, Ford Focus Electric, Mitsubishi Outlander PHEV, Kia Soul EV, Nissan Leaf 2012–2017, Peugeot, Toyota Prius, and Vauxhall. The plot corresponds to different cycle numbers during charging, of which the curves change with ageing. Inspection of Figure 7 shows that the voltage vs. *SOC* curves shrunk with decrease in *SOC*. *SOC* decreased with the increase in cycle number. The reduction in the *SOC* axis happened due to the loss of active material (LAM) and lithium inventory (LLI), and the reduction in the VOC axis happened due to the increase in internal resistance. The internal resistance increased with ageing mostly due to the increase in SEI layer on the anode surface. According to the data shown in Figure 7, we applied the data fitting using the parameters shown in Table 2 and obtained the VOC-*SOC* plot according to our shifted sigmoid model as solid lines shown in Figure 7. The ageing effect after many cycles of charging moved both the $V_{OC,MAX}$ and the peak capacitance voltage V_P to the higher voltages and reduced the c_{max} simultaneously as shown in Table 2. Loss of active material results in permanent capacity Q reduction in the battery. The focus factor α and the scaling factor K were calculated from Equations (12) and (13) iteratively. There is difference a between the experimental data [19] and the model fitting according to Equation (1). The difference may be due to the shifted sigmoid model in Equation (1); the VOC-*SOC* modeling does not have not enough degrees of freedom to perform the best fit. The other reason may result from the experiment data acquisition. The charging current depending on the charging rate is converted into *SOC* at each sampling time, which fluctuates in the beginning and thus the integration from the current reading is not accurate in the initial stage of *SOC* calculation.

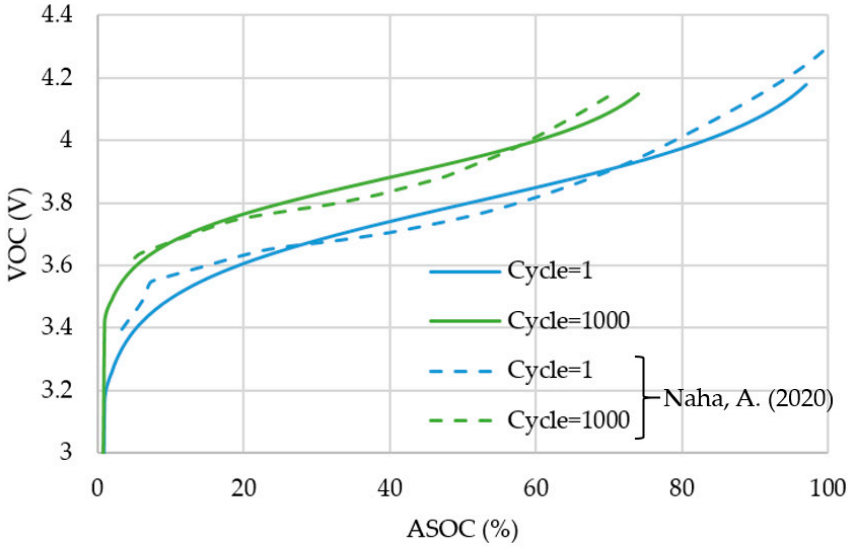

Figure 7. Model fitting of cycle tests of Type-1 battery compared to the dotted lines obtained from [19].

Table 2. Parameters for Type-1 batteries.

Symbol	Unit	Cycle 1 Value	Cycle 1000 Value
Q	Ah	3	2.1
c_{max}	Ah/V	5.8	4.9
$V_{OC,MAX}$	V	4.4	4.6
V_P	V	3.88	3.88
α		7.883388	9.31
K		1.034	1.001

3.3. Constant Current Charging

The battery internal resistance R_i due to the increase in thickness of the solid–electrolyte interface (SEI) layer increased along the charge/discharge cycle number, and the battery voltage as shown in Figure 8a during charge/discharge may be written as follows.

$$V_{CH} = V_{OC} \pm I_{CH} \cdot R_i \tag{21}$$

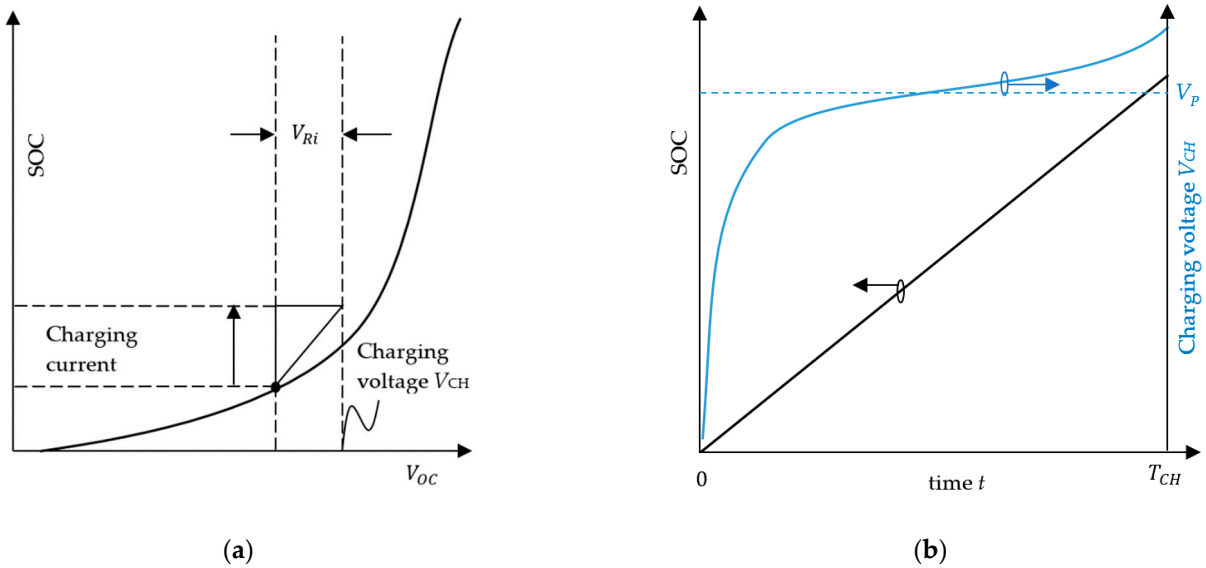

Figure 8. Constant current charging (**a**) *SOC* to voltage and (**b**) charging function.

I_{CH} denotes the charging or discharging current. During first charge, assuming the internal resistance remains constant within the charge time T_{CH}, Equation (21), during the charging period, has a positive current sign. The time required to charge the battery from zero voltage to the open circuit voltage V_{OC} depends on the state of charge. We call the charging process the constant current charging when the state of charge is controlled so that it increases linearly in the function of time as follows. The *SOC* during constant current charging time t yields an expression as follows.

$$SOC(t) = 100\% \times g = 100\% \times \frac{t}{T_{CH}} \tag{22}$$

The above equation can be subsequently equated as follows.

$$\frac{t(V_{OC})}{T_{CH}} = \int_0^t g(t)d\tau = \int_0^t g' \frac{dv_{OC}}{d\tau} d\tau = \int_0^{V_{OC}} g' dv_{OC} = g(V_{OC}) \tag{23}$$

The open-circuit voltage V_{OC} during constant current charging is then derived according to Equation (17) as follows.

$$V_{OC}(t) = \frac{1}{\alpha} ln\left(\frac{t}{KT_{CH} - t}\right) + V_P \tag{24}$$

As shown in Figure 8b, the control charging voltage function $V_{CH}(t)$ can be considered taking the similar sigmoid function form as follows.

$$V_{CH}(t) = V_{OC}(t) + I_{CH}R_i \tag{25}$$

The $V_{CH}(t)$ is increased rapidly in the beginning time due to the natural logarithm function in Equation (24), and can increase fast from t = 0, though at the end of the time as t approaches T_{CH} the natural logarithm term will increase again, which is the shifted sigmoid function.

Considered with a microprocessor or FPGA based discrete control scheme, the charging voltage v_{CH} may use a proportional controller with the current feedback in discrete form as follows.

$$v_{CH}(k) = v_{CH}(k-1) + G_p R_i (I_{CH} - i_{BAT}(k-1)) \tag{26}$$

I_{CH} is the desired constant current to charge into the battery. G_p is the proportional control gain. Small letter k is the tick count, which denotes the k-th time count in the sampling time of T_S as a discrete control convention. Due to the ion mobility increase as temperature rises, the internal resistance is reduced at high temperatures, which is known as the negative thermal coefficient resistor effect. The internal resistance R_i excluding the solid–electrolyte interface resistance R_{SEI} is known as the negative temperature coefficient for the lithium batteries, which is recommended at -10 °C as its nominal value. i_{BAT} is the charging current at the instance of time. The voltage drop on the internal resistance is written as follows.

$$v_{Ri} = R_i \times i_{BAT} \tag{27}$$

Equation (26) is then reformulated in the voltage form as follows, which is independent of V_{OC}.

$$v_{CH}(k) = v_{CH}(k-1) + G_p R_i I_{CH} - G_p v_{Ri}(k-1) \tag{28}$$

Equations (24) and (28) are different in the real-time and discrete-time form expression; we obtain the same value at the same time tick count k as follows.

$$v_{CH}(k) = V_{CH}(t) \tag{29}$$

We may simulate the $v_{CH}(k)$ process according to Figure 8 and plot the voltage changes due to each time tick as shown in Figure 9. During constant current charging under the discrete control, the fixed height of the rectangular boxes is the constant charging current due to Equation (22). The constant current increases the *SOC* incrementally after each time tick. On the other hand, the voltage increment which is the width of the rectangular boxes gradually decreases. The voltage function is shown in Equation (24) and Figure 8b. The reciprocal of the rate of change of the voltage is shown in the blue curve, which is the same with the instantaneous capacitance due to the constant current charging as follows.

$$c = I_{CH}\frac{T_s}{\Delta V_{OC}} \tag{30}$$

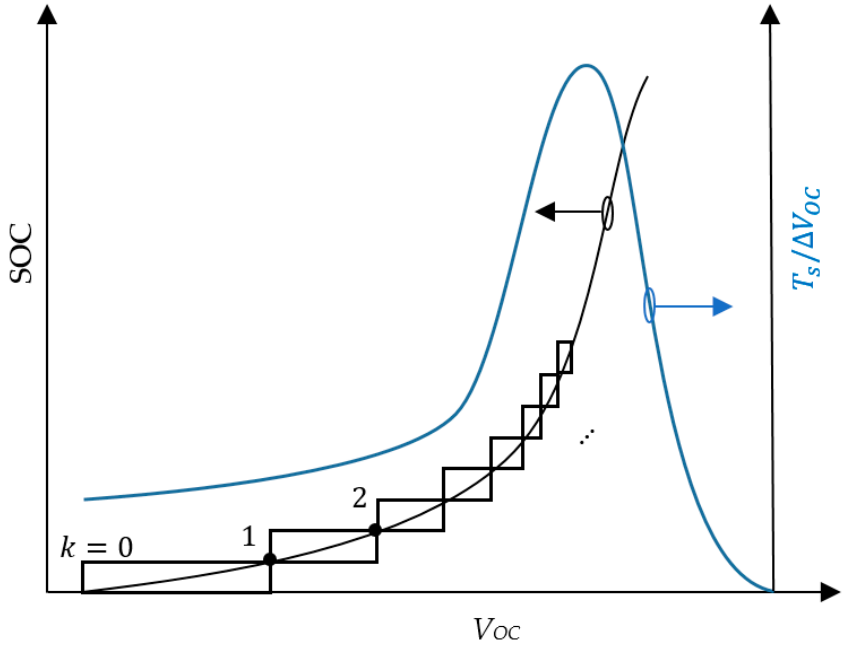

Figure 9. The reciprocal of charging voltage slew rate in constant current charging.

The above equation is in consistent with Equation (7). The voltage slew rate increases again after V_P.

3.4. Charging Parallel Connected Batteries

According to the derived result from the previous sections, the parallel connected batteries with two different peak capacitance voltages present different voltage slew rates about their individual V_P's. The batteries' voltage, after ageing both the maximum open circuit voltage and the peak capacitance, can become higher than the new one as shown in Table 2; however, the maximum instantaneous capacitance also decreases due to the ageing. The mismatch between two batteries causes unbalance on the batteries during parallel charging. The active cell-balancing method of serially connected batteries is proposed, such as the multi-winding flyback to charge the batteries using flyback converter to balance the charges in the batteries. It is actually the parallel charging via the magnetic field.

When two batteries are connected in parallel without any charging current, it can be assumed that the charges are rapidly balanced between batteries until the internal current flow is zero. When there is no more charge redistribution between the batteries, they shall share the same voltage $V_{OC,1} = V_{OC,2}$ with different *SOC* as follows.

$$\frac{1}{\alpha_2}ln\left(\frac{g_2}{K_2 - g_2}\right) - \frac{1}{\alpha_1}ln\left(\frac{g_1}{K_1 - g_1}\right) = V_{P,1} - V_{P,2} \tag{31}$$

During the charging process, however there is non-zero internal current flow between two batteries due to the instantaneous capacitance differences. Assuming that the internal resistance are the identical, $R_{i,1} = R_{i,2} = R_i$, the internal current is the difference of two branch currents as follows.

$$i_{CH,1} - i_{CH,2} = \frac{1}{R_i}\left(c_2\dot{v}_{OC,2} - c_1\dot{v}_{OC,1}\right) + \frac{1}{R_i}(v_{oc,2} - v_{oc,1}) \tag{32}$$

As stated in the previous sections, the battery with larger cycle number can result in higher maximum instantaneous capacitance. Assuming the circuit has some inductance that maintains $\dot{v}_{OC} = \dot{v}_{OC,1} \approx \dot{v}_{OC,2}$ we can rewrite the above equation into as follows.

$$i_{CH,1} - i_{CH,2} = \frac{1}{R_i}\left(Q_2{g_2}' - Q_1{g_1}'\right)\dot{v}_{OC} + \frac{1}{R_i}(v_{oc,2} - v_{oc,1}) \tag{33}$$

The internal current $i_{CH,2}$–$i_{CH,1}$ between two parallel connected batteries is affected by the mismatching of batteries due to ageing which decreases both the capacity Q and the peak capacitance voltage. Summation of the two currents is the overall charging current at the k sampling time as follows.

$$I_{CH} = i_{CH,1}(k) + i_{CH,2}(k) \tag{34}$$

Following the similar parameter reasoning as shown in Table 2, Battery 2 is the battery with cycle = 1000. As a result, Battery 2 can be not fully charged when the charging voltage reaches the maximum open circuit voltage which is $V_{OC,MAX,1}$ since Battery 1 is a new battery. It will leave behind some *SOC* difference for Battery 2 as follows.

$$SOC_2 = 100 \cdot (1 - g_2) = 100 \cdot \frac{e^{-\alpha_2 V_{OC,MAX,1}} + (1 - K_2)e^{-\alpha_2 V_{P,2}}}{e^{-\alpha_2 V_{OC,MAX,1}} + e^{-\alpha_2 V_{P,2}}} \tag{35}$$

4. Simulation and Experiments

In the simulation, we used the case study provided in Table 2 with only two single batteries connected in parallel during charging. In the experiment, we charged 12 V ternary batteries connected in S3P2.

4.1. Simulation

We analyzed the parallel charging of two batteries as with parameters as shown in Table 2 [19] as an extreme case study which includes two batteries: one was brand new and the other was exhaustively used. Other parameters associated with the constant current control are shown in Table 3. For parallel battery charging, the control law uses the sensor feedback of the two batteries.

$$v_{CH}(k) = \frac{v_{OC,1}(k) + v_{OC,2}(k)}{2} + G_p(I_{CH,cmd} - I_{CH}(k)) \tag{36}$$

where

$$\begin{array}{c} v_{OC,m}(k) = v_{CH}(k-1) - i_{CH,m}(k-1)R_{i,m},\ m = 1,\ 2 \\ I_{CH}(k) = i_{CH,1}(k) + i_{CH,2}(k) \end{array}. \tag{37}$$

The internal resistance increases with the battery temperature associated with the current as follows.

$$R_{i,m} = R_i + |i_m| \cdot \delta R \tag{38}$$

The initial *SOC* in terms of the individual shifted sigmoid functions g_m are derived from Equation (31). When there was no more charge redistribution, we started to perform the constant current control as stated in Equation (36). The simulation of individual charging currents of two batteries is shown in Figure 10. In this extreme case using two very different age batteries, it is shown that the parallel charging surged a large current on

the elder battery with cycle = 1000 in the initial stage of charging. The current surge was almost 50% of the average current, which was due to the cycle = 1 battery (or the younger battery) having a higher *SOC* compared with the cycle = 1000 battery (or the elder battery) according to Equation (1) initially. The difference of the two *SOC*'s can be verified through Equation (31) and shown in Table 3. In the beginning 2 min (k = 0 to 5), the younger battery indeed charged the elder one. However, after the first 2 min the younger battery started a charging curve such, as shown in Figure 8b, to increase the open circuit voltage, as shown in Figure 10b, via increasing the current. On the other hand, the elder battery decreased the current of charge after the first 2 min. There was a crossing point between the elder battery with the younger one as shown in Figure 10a.

Table 3. Parameters used in the constant current charging simulation.

Symbol	Unit	Value	Cycle 1 Value	Cycle 1000 Value
G_p		0.02		
R_i	mΩ	80		
δR	mΩ/Ampere			
$I_{CH,cmd}$	A	20		
$v_{OC,1}(0) = v_{OC,2}(0)$	V	3.7		
$g_1(0)$		0.2		
$g_2(0)$		0.06		
Sampling time T_S	S	30		
Q	Ah		7	6
c_{max}	Ah/V		12	9
$V_{OC,MAX}$	V		4.7	4.9
V_P	V		3.8	3.9
α			7	9
K			1	1

According to the time tick, the crossing point was around 30 min (k = 65) after the beginning of charging. After the crossing point, the younger battery started to have a higher current than the elder one. At a certain time, which was 1 h and 40 min (k = 100) in this study case, the elder battery reached its open circuit voltage limit and the charging current stopped. This is the other problem which occurred for the younger battery since when the elder battery does not need more current to charge, but the constant current charging law in Equation (36) still holds and caused a rapid current rise on the younger battery.

From the thermal point of view, due to the heat generated by the internal resistance, the battery set became hot during the initial stage before $k < 5$ and the final stage after $k > 200$ during the heat dissipation proportional to the current square. From Figure 10b, it is also observed that the assumption applied to Equation (33) was challenged on the time tick at k = 0 and k = 200 when rest of the time Equation (33) was used in the approximation. From Equation (33), we read that the higher the open circuit voltage in the battery, the lower the current flowing into the same battery. The open circuit voltage on the elder battery was higher than the younger one after $k > 200$, hence the current of the elder battery was lower. However, there is the other term in Equation (33), that is, the higher the instantaneous capacitance of the battery, the lower the current flowing into the same battery. It is the reason why the current flowing into the younger battery before $k < 200$ was smaller than the elder one. During the constant current control, the charging voltage $v_{CH}(k)$ increased according to Equation (36) to maintain the constant current. In the typical charging control strategy, the constant voltage charging is applied when the charging voltage $v_{CH}(k)$ reaches the voltage limit.

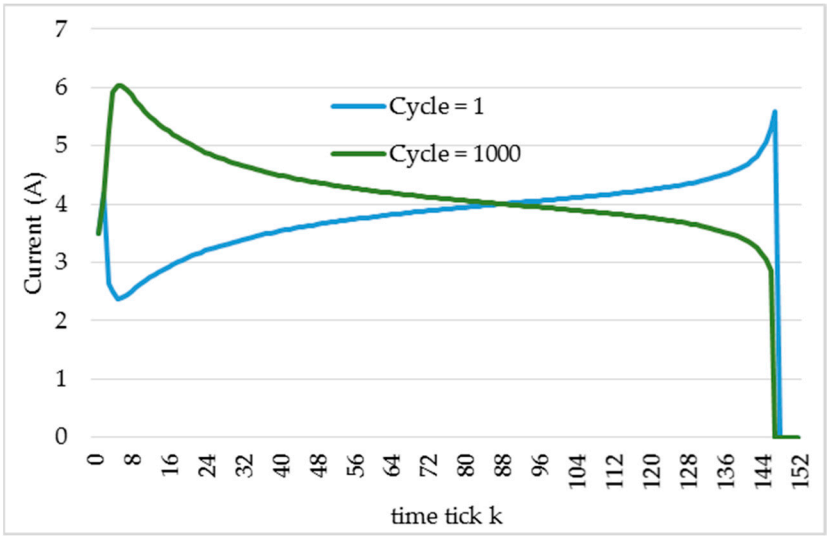

(**a**)

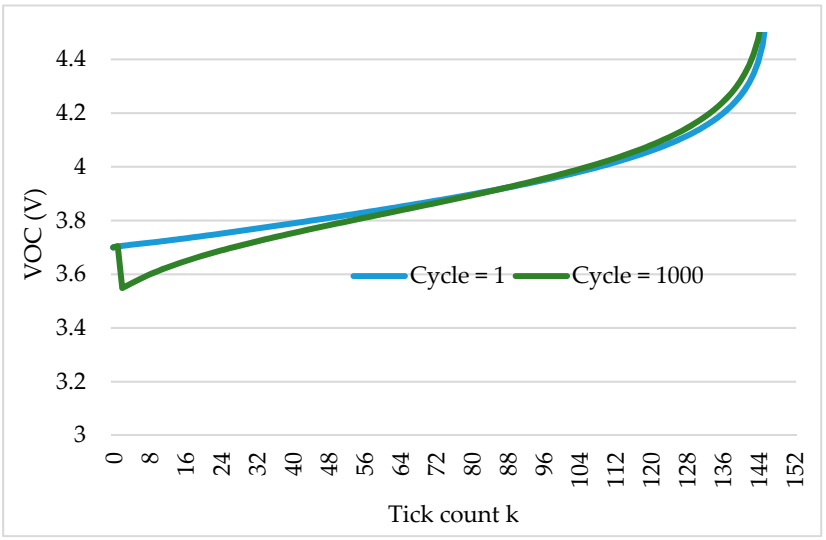

(**b**)

Figure 10. Simulation of parallel charging; (**a**) the current responses and (**b**) the voltage responses on different branches.

4.2. Experiments

In the experiment, we chose six 18,650 ternary batteries from A + plus Co. and performed the *SOC* test using ZKETech EBDAH DC Electronics load and its software. The capacity of the battery right after manufacturing is 2.6 Ah. The *SOC*–VOC results are shown in Figure 11. The charging circuit used the interleaved flyback converter as shown in Figure 2, though only one secondary side was necessary for the small current charging. In the experiment, we charged 12 V ternary batteries connected in S3P2. We connected three batteries #1, #2, and #3 in series from Figure 11a into one battery string. The other battery string consists of #4, #5, and #6. The charging is 0.65 C and the charging period is 90 min. Table 4 shows the parameters for different ternary battery cells. Among all cells, the #6 cell is an aging cell, which has only one half of maximum instantaneous capacitance C_{max} of all others. The #6 cell particularly was chosen to represent the anomaly in the S3P2 battery pack. This abnormal battery cell can cause the entire battery string (#4, #5, #6) behave as an older battery string due to the total capacitance of capacitors in the series being no greater than the smallest capacitance of all capacitors.

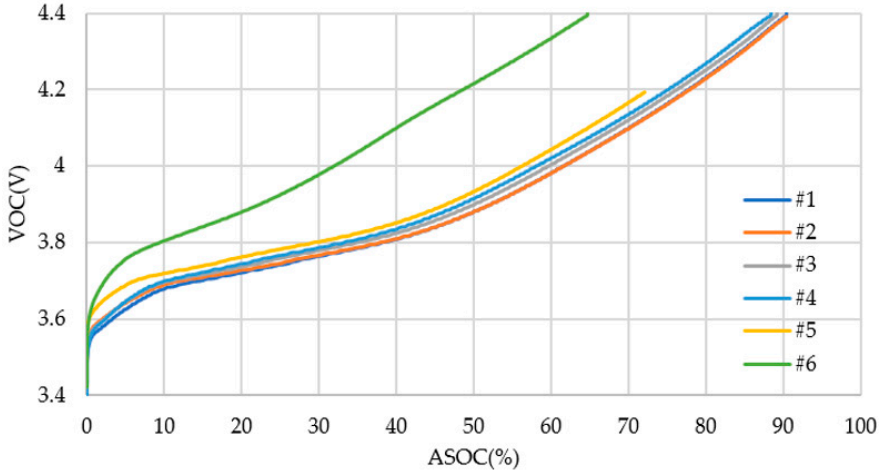

(**a**)

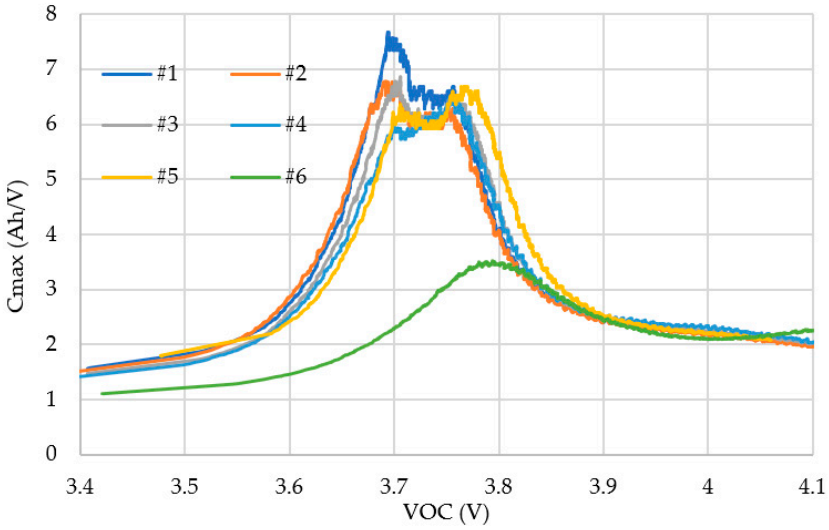

(**b**)

Figure 11. 18,650 Ternary battery (**a**) *SOC*–VOC curve and (**b**) C_{max}–VOC curve.

Table 4. Parameters for ternary batteries.

Symbol	Unit	#1–#4 Nominal Value	#5 Value	#6 Value
Q	Ah	2.35	2.3	2
c_{max}	Ah/V	6	5.8	3.5
$V_{OC,MAX}$	V	4.7	4.72	4.8
V_P	V	3.75	3.77	3.9
α		10.20	10.09	7
K		1	1	1

The experiment setup was designed, implemented, and tested and is shown in Figure 12a, including the lithium-ion battery module and the interleaved flyback converter circuit. The input DC voltage of the converter on the primary side is 72 V. The standard charging protocol for lithium-ion batteries is constant-current constant-voltage (CCCV), but it brings some drawbacks such as the overcharging and the extended charging time. In order to solve the above problems, our charging protocol chose the positive pulse current charging for charging LIBS instead of traditional charging methods. In addition, the pulse current charging provides several extra advantages such as longer battery life span and low degradation of the battery material. The charging current results for the

individual battery string were recorded from 11 V to 13 V as shown in Figure 12b. We observed that the result of the charging time from 10 to 60 min matched the simulation result in Figure 10. The older battery string (#4, #5, #6) surged a high current at beginning, fell to the intersection later, and the charging current decreased continuously to the end of the charging period. Conversely, according to the Equations (33) and (34), the younger battery string (#1, #2, #3) was charged with smaller current than that of the older battery string (#4, #5, #6) in the beginning and rose to a higher current at the end.

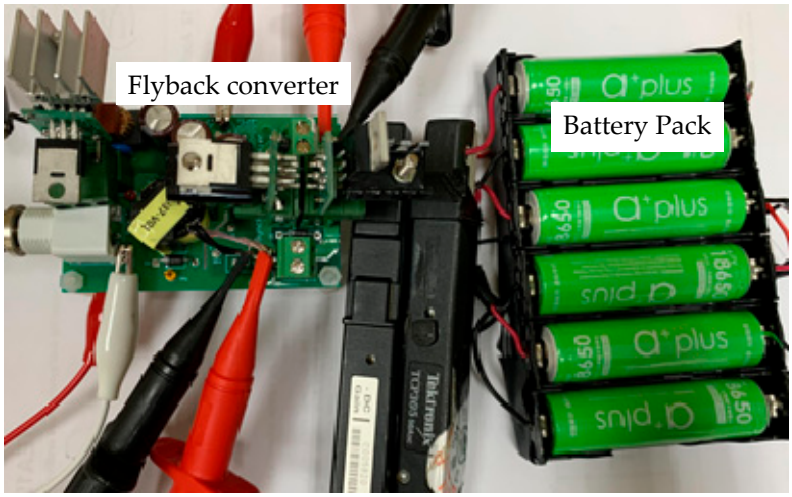

(**a**)

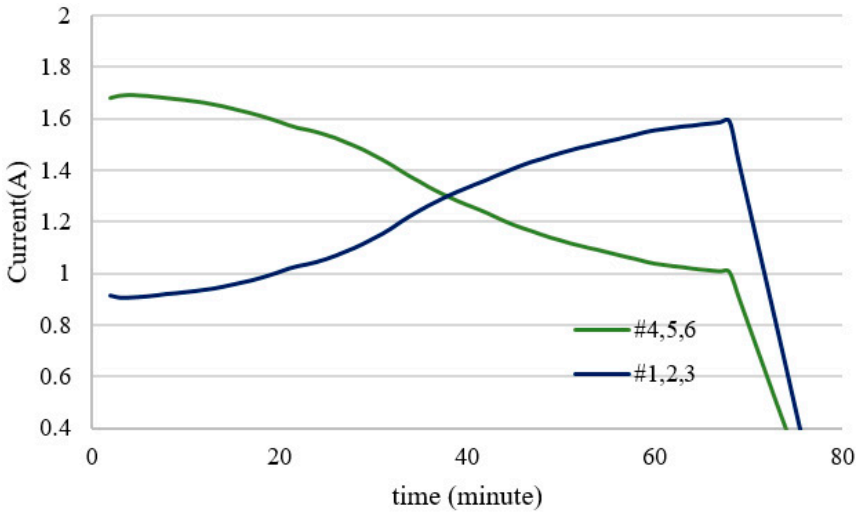

(**b**)

Figure 12. Parallel lithium battery charging experiment: (**a**) experimental setting and (**b**) 1.3 A current response.

The individual VOC, V_S, i_S, and $i_{\#4,5,6}$ are shown in Figure 13 and the other battery string $i_{\#1,2,3}$ can be obtained by subtracting $i_{\#4,5,6}$ from the secondary side current i_S of the flyback converter. The operation frequency and duty cycle of the converter were 280 kHz and 60% respectively. It can be seen that the maximum current on the secondary side of the flyback converter was 10 A for charging two parallel battery strings with 1.3 A average current on each individual battery string. For even more parallel battery strings, the interleaved flyback converter is needed to improve the power conversion efficiency due to the excessive amount of current causing large resistive loss on the flyback converter.

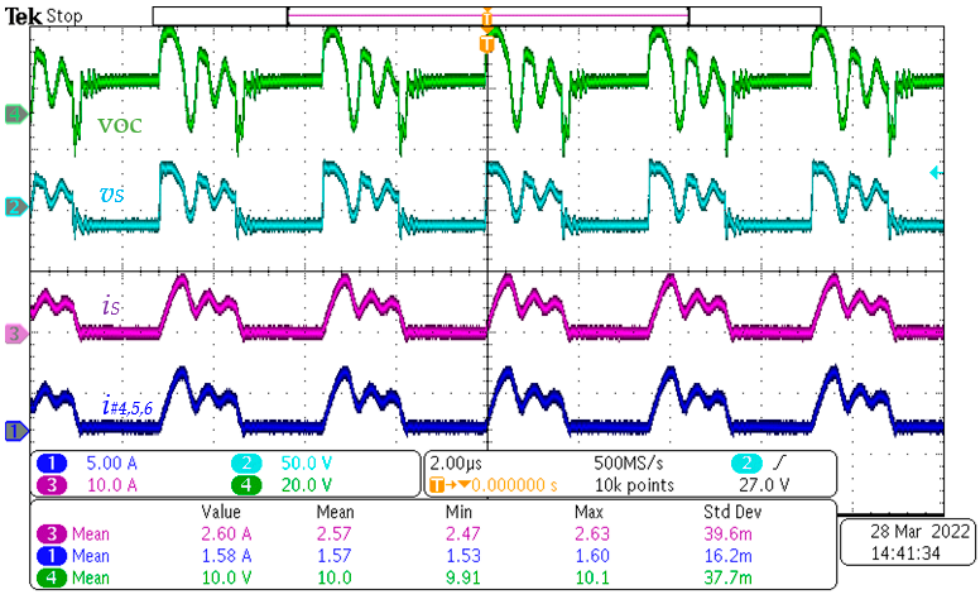

Figure 13. Waveforms of battery charging with 12 V/2.6 A on the secondary side using the flyback converter.

5. Discussion

The VOC-*SOC* model stated in Equation (1) has three parameters α, K, and V_P. These parameters are subsequently related to the physical quantities including the charge capacity Q and the maximum instantaneous capacitance C_{max}, and the maximum open circuit voltage $V_{OC,MAX}$ using Equations (12) and (13). In order to compare the proposed model with other known models [20,21], we may convert the model reversely that the open circuit voltage VOC is written in terms of *SOC* [21]. We first define the symbol s to denote the shifted sigmoid function as follows.

$$s \equiv g(V_{OC}) \tag{39}$$

Equation (39) is then rewritten into the expression as follows.

$$V_{OC} = V_P + \frac{1}{\alpha}\ln(s) - \frac{1}{\alpha}\ln(K - s) \tag{40}$$

Equation (40) matches the Nernst model except for the parameter K, which is expressed in terms of the physical quantities as stated in Equation (13). Only for those batteries with large capacity Q does the corresponding parameter K approach unity. The range of parameter K is stated in Equation (5), which is between 1 and 2. According to the experimental data, we can start from providing the initial guess of K and perform the fitting using the shape functions 1, $ln(s)$, and $ln(K - s)$ to obtain the physical quantities Q, C_{max}, and $V_{OC,MAX}$. The physical quantities are then substituted into Equation (13) until the value of K converges. As stated in Section 3.1, these three parameters are functions of temperature and aging conditions. The model fitting is applied to different operating temperatures [21]. The parameters α, K, and V_P obtained from the model fitting as shown in Table 5 are not with many differences. The physical quantities C_{max} and $V_{OC,MAX}$ had some changes, among which the charge capacity C_{max} became lower for the low temperature shown in Figure 14.

Table 5. Parameters under different operating temperatures.

Symbol	Unit	−10 °C	50 °C
		Value	Value
Q	Ah	1.5	1.5
C_{max}	V	3.33	3.8
$V_{OC,MAX}$	V	4.5	4.5
V_P	Ah/V	3.88	3.86
α		8.88	10.1
K		1.004	1.0015

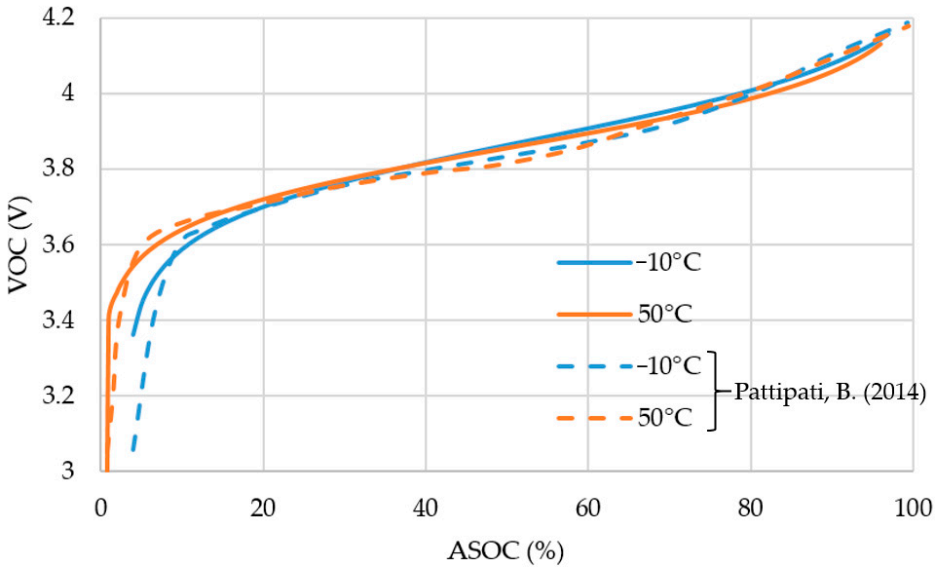

Figure 14. Proposed model fitting under different operating temperatures [21].

It is very difficult to maintain a balanced *SOC* for each battery in multiple battery modules, which directly determines the discharge capacity of the battery module. Using the flyback converter can only ensure that the amount of charge charged in the same charging stage is the same. It is still required with passive and active cell balancing [22] to allow each cell in the battery pack to be monitored to maintain a healthy battery state of charge (*SOC*) during charging. This extends battery cycle life and provides additional protection by preventing damage from overcharging. Current inconsistencies during parallel charging were found in both the initial and final stages of charging, shown in the results from both Figures 10 and 12. There are pre-balancing methods known to resolve the current inconsistency problems in the initial stage of charging. For the current inconsistencies in the final stage of the charging, it is typically recommended to use the CCCV control, that is, the constant voltage control is applied after a certain *SOC*% is reached. In different application scenarios such as temperature and the charging rate in C, the internal resistance can change, the charge capacity Q and the maximum instantaneous capacitance C_{max}, and the maximum open circuit voltage $V_{OC,MAX}$ can change as well. The *SOC* estimation can yield a nominal range for the normal cells subjected to different application scenario, which allows the anomaly detection in the BMS and yields guidance for passive balancing solutions for battery pack protection.

6. Conclusions

In this paper, we explained the unbalanced current mechanism occurring in parallel lithium battery charging during constant current charging using the proposed *SOC*–VOC mathematical model. The *SOC*–VOC mathematical model explained why the unbalanced current does not only occur in the beginning of the parallel charging but also the end of battery charging. This is also the reason why the temperature of the batteries rises

during the starting and the finishing stages of charging. The old battery was observed with a smaller total charge, lower maximum instantaneous capacitance, higher open circuit voltage, and higher peak voltage based on the *SOC*–VOC mathematical model fitting. The anomaly condition as well as the cell inconsistency of the cells in the battery pack may be detected according to these four parameters obtained from the *SOC*–VOC model fitting. The four parameters of the battery can also be used to categorize various kinds of batteries. It is then useful for designing the passive protection such as current sense resistors, resettable thermal cutoff devices, or resettable fuses. A special interest being under development in NYCU IME laboratory is the passive current limiting device using the D-mode GaN HEMT, which relies on the mathematical modeling of the battery including the peak voltage and lower maximum instantaneous capacitance. The advances of battery protection using this mathematical model will be reported in the future.

Author Contributions: Conceptualization, E.-Y.C. and W.-H.C.; methodology, S.-L.J., Y.-T.S. and C.-C.W.; software, C.-C.W.; validation, C.-Y.L. and Y.-T.S.; formal analysis, Y.-S.S.; writing—original draft preparation, S.-L.J. and W.-H.C.; writing—review and editing, Y.-T.S., C.-Y.L., Y.-T.S. and C.-C.W.; visualization, C.-Y.L. and C.-C.W.; supervision, E.-Y.C.; project administration, W.-H.C.; funding acquisition, W.-H.C. and E.-Y.C. All authors have read and agreed to the published version of the manuscript.

Funding: This research was funded by Ministry of Science and Technology, R.O.C, grant number MOST(NSC) 110-2622-8-009-018-SB; MOST(NSC) 110-2622-8-007-019. In part, this work was also financially supported by the "Center for the Semiconductor Technology Research" from The Featured Areas Research Center Program within the framework of the Higher Education Sprout Project by the Ministry of Education (MOE) in Taiwan. Also supported in part by the Ministry of Science and Technology, Taiwan, under Grant MOST 110-2634-F-009-027.

Institutional Review Board Statement: Not applicable.

Informed Consent Statement: Not applicable.

Data Availability Statement: Data sharing is not applicable.

Acknowledgments: This work was supported by the Ministry of Science and Technology, R.O.C. The authors also thank You-Chen Weng of the CSD Lab for fabricating the D-Mode MIS-HEMT chips and IMLab graduate student Rohit Roy for his help in the manuscript editing.

Conflicts of Interest: The authors declare no conflict of interest.

References

1. Sun, F.; Xiong, R. A novel dual-scale cell state-of-charge estimation approach for series-connected battery pack used in electric vehicles. *J. Power Source* **2015**, *274*, 582–594. [CrossRef]
2. Bruen, T.; Marco, J. Modelling and experimental evaluation of parallel connected lithium ion cells for an electric vehicle battery system. *J. Power Source* **2016**, *310*, 91–101. [CrossRef]
3. Bui, T.M.; Kim, C.-H.; Kim, K.-H.; Rhee, S.B. A Modular Cell Balancer Based on Multi-Winding Transformer and Switched-Capacitor Circuits for a Series-Connected Battery String in Electric Vehicles. *Appl. Sci.* **2018**, *8*, 1278. [CrossRef]
4. Ramos-Paja, C.A.; Bastidas-Rodriguez, J.D.; Saavedra-Montes, A.J. Design and Control of a Battery Charger/Discharger Based on the Flyback Topology. *Appl. Sci.* **2021**, *11*, 10506. [CrossRef]
5. Guo, X.; Geng, J.; Liu, Z.; Xu, X.; Cao, W. A Flyback Converter-Based Hybrid Balancing Method for Series-Connected Battery Pack in Electric Vehicles. *IEEE Trans. Veh. Technol.* **2021**, *70*, 6626–6635. [CrossRef]
6. Imtiaz, A.M.; Khan, F.H. "Time shared flyback converter" based regenerative cell balancing technique for series connected Li-ion battery strings. *IEEE Trans. Power Electron.* **2013**, *28*, 5960–5975. [CrossRef]
7. Shrivastava, P.; Soon, T.K.; Idris, M.Y.I.B.; Mekhilef, S. Overview of model-based online state-of-charge estimation using Kalman filter family for lithium-ion batteries. *Renew. Sustain. Energy Rev.* **2019**, *113*, 109233. [CrossRef]
8. Elmahdi, F.; Ismail, L.; Noureddine, M. Fitting the VOC-SOC relationship of a battery lithium-ion using genetic algorithm method. In *E3S Web of Conferences*; EDP Sciences: Les Ulis, France, 2021; Volume 234.
9. Han, X.; Feng, X.; Ouyang, M.; Lu, L.; Li, J.; Zheng, Y.; Li, Z. A comparative study of charging voltage curve analysis and state of health estimation of lithium-ion batteries in electric vehicle. *Automot. Innov.* **2019**, *2*, 263–275. [CrossRef]
10. He, Y.J.; Shen, J.N.; Shen, J.F.; Ma, Z.F. Embedding monotonicity in the construction of polynomial open-circuit voltage model for lithium-ion batteries: A semi-infinite programming formulation approach. *Ind. Eng. Chem. Res.* **2015**, *54*, 3167–3174. [CrossRef]

11. Weng, C.; Sun, J.; Peng, H. A unified open-circuit-voltage model of lithium-ion batteries for state-of-charge estimation and state-of-health monitoring. *J. Power Source* **2014**, *258*, 228–237. [CrossRef]
12. Deng, Q.; Lin, B. Automated machine learning structure-composition-property relationships of perovskite materials for energy conversion and storage. *Energy Mater.* **2021**, *1*, 100006. [CrossRef]
13. Liang, J.; Wu, T.; Wang, Z.; Yu, Y.; Hu, L.; Li, H.; Zhang, X.; Zhu, X.; Zhao, Y. Accelerating perovskite materials discovery and correlated energy applications through artificial intelligence. *Energy Mater.* **2022**, *2*, 200016. [CrossRef]
14. Wassiliadis, N.; Schneider, J.; Frank, A.; Wildfeuer, L.; Lin, X.; Jossen, A.; Lienkamp, M. Review of fast charging strategies for lithium-ion battery systems and their applicability for battery electric vehicles. *J. Energy Storage* **2021**, *44*, 103306. [CrossRef]
15. Murdock, B.E.; Toghill, K.E.; Tapia-Ruiz, N. A Perspective on the Sustainability of Cathode Materials used in Lithium-Ion Batteries. *Adv. Energy Mater.* **2021**, *11*, 2102028. [CrossRef]
16. Das, A.; Li, D.; Williams, D.; Greenwood, D. Joining Technologies for Automotive Battery Systems Manufacturing. *World Electr. Veh. J.* **2018**, *9*, 22. [CrossRef]
17. Tomaszewska, A.; Chu, Z.; Feng, X.; O'Kane, S.; Liu, X.; Chen, J.; Ji, C.; Endler, E.; Li, R.; Liu, L.; et al. Lithium-ion battery fast charging: A review. *eTransportation* **2019**, *1*, 100011. [CrossRef]
18. Lodh, T.; Pragallapati, N.; Agarwal, V. Novel control scheme for an interleaved flyback converter based solar PV microinverter to achieve high efficiency. *IEEE Trans. Ind. Appl.* **2018**, *54*, 3473–3482. [CrossRef]
19. Naha, A.; Han, S.; Agarwal, S.; Guha, A.; Khandelwal, A.; Tagade, P.; Hariharan, K.S.; Kolake, S.M.; Yoon, J.; Oh, B. An incremental voltage difference based technique for online state of health estimation of li-ion batteries. *Sci. Rep.* **2020**, *10*, 9526. [CrossRef] [PubMed]
20. Das, R.; Wang, Y.; Putrus, G.; Busawon, K. Modelling the State of Charge of Lithium-ion batteries. In Proceedings of the 2018 53rd International Universities Power Engineering Conference (UPEC), Glasgow, UK, 4–7 September 2018; pp. 1–6.
21. Pattipati, B.; Balasingam, B.; Avvari, G.V.; Pattipati, K.R.; Bar-Shalom, Y. Open circuit voltage characterization of lithium-ion batteries. *J. Power Source* **2014**, *269*, 317–333. [CrossRef]
22. Scott, K.; Nork, S. *Active Battery Cell Balancing*; Technical Article; Analog Devices, Inc.: München, Germany, 2019; Available online: http://www.analog.com/en/technical-articles/active-battery-cell-balancing.html (accessed on 26 June 2022).